

# The secreted kinase ROP17 promotes *Toxoplasma gondii* dissemination by hijacking monocyte tissue migration

Lisa L. Drewry<sup>1</sup>, Nathaniel G. Jones<sup>1,4</sup>, Quiling Wang<sup>1</sup>, Michael D. Onken<sup>2</sup>, Mark J. Miller<sup>3</sup> and L. David Sibley<sup>1\*</sup>

**The protozoan parasite *Toxoplasma gondii* is thought to exploit monocyte trafficking to facilitate dissemination across endothelial barriers such as the blood–brain barrier. Here, we analysed the migration of parasitized monocytes in model endothelial and interstitial environments. We report that infection enhanced monocyte locomotion on the surface of endothelial cells, but profoundly inhibited monocyte transmigration across endothelial barriers. By contrast, infection robustly increased monocyte and macrophage migration through collagen-rich tissues in a Rho–ROCK-dependent manner consistent with integrin-independent interstitial migration. We further demonstrated that the secreted *T. gondii* protein kinase ROP17 was required for enhanced tissue migration. In vivo, ROP17-deficient parasites failed to upregulate monocyte tissue migration and exhibited an early dissemination delay, leading to prolonged mouse survival. Our findings indicate that the parasite-induced changes in monocyte motility primarily facilitate the transport of *T. gondii* through tissues and promote systemic dissemination, rather than shuttle parasites across the blood–brain barrier via extravasation.**

The protozoan parasite *Toxoplasma gondii* causes severe disease in immunocompromised humans<sup>1</sup> and is among the few pathogens that invades the central nervous system (CNS) by crossing the blood–brain barrier (BBB). *T. gondii* is theorized to hijack leukocytes as shuttles that enable extravasation across the BBB<sup>2,3</sup>. Infected leukocytes could also aid dissemination at several other infection stages. After oral ingestion, parasites traverse the intestinal epithelium and enter the lamina propria<sup>4,5</sup>, thus immediately encountering resident phagocytes<sup>3,6,7</sup> and later recruited inflammatory monocytes<sup>8</sup>. From this infection nidus, parasites disseminate to draining lymph nodes, the blood, spleen and, eventually, all organs including the brain<sup>4,5,9</sup>. Infected leukocytes could promote dissemination by carrying parasites out of the lamina propria, through the lymphatic vasculature and into the circulation. Circulating leukocytes could also deliver parasites across endothelial barriers and into new tissues via extravasation, a sequential process that is initiated by selectin-mediated leukocyte capture, progresses to integrin-based adhesion and vascular crawling, and commences with endothelial traversal<sup>10</sup>.

As one of the most severe complications of toxoplasmosis is encephalitis<sup>1</sup>, the potential for extravasating leukocytes to ferry parasites across the BBB has been keenly investigated<sup>9,11</sup>. In vitro modeling of this process revealed that parasite infection enhanced primary human monocyte crawling on human umbilical vein endothelial cells (HUVECs) without significantly altering transendothelial migration (TEM)<sup>12,13</sup>. These findings prompted a proposal that infected monocytes are poised to deliver parasites across the BBB<sup>3,14</sup>. However, infection diminished integrin-mediated endothelial adherence<sup>15,16</sup>, a step generally considered prerequisite to endothelial crawling and transmigration<sup>10</sup>. Numerous reports have shown that *T. gondii*-infected

dendritic cells exhibit hypermigratory behaviour<sup>17–20</sup>. However, during murine infection, nearly all parasitized leukocytes in the blood are CD11b<sup>+</sup> monocytes<sup>11</sup>. Consistent with a role for monocytes in dissemination, adoptive transfer of infected monocytes hastens dissemination to the CNS in mice<sup>11</sup>. However, a different conclusion was reached by a recent study assessing the potential for blood-localized extracellular parasites to invade the mouse CNS, which noted that adoptively transferred infected monocytes were readily detected in the brain vasculature but not in the parenchyma<sup>9</sup>. In total, current data are inconsistent with a simple model in which infected monocytes are the primary vehicle for parasites to cross the BBB.

Here, we examine how infected monocytes migrate using in vitro models that mimic vascular versus tissue environments. We found that infection inhibited transmigration across the BBB and peripheral endothelium, processes that require integrin-dependent adhesion. By contrast, infection enhanced monocyte and macrophage migration through collagen-rich tissues, distinct environments that support integrin-independent motility. The tissue migration of parasitized monocytes and macrophages required host Rho–Rho-associated protein kinase (ROCK) signalling, and the secreted parasite kinase ROP17, which was also required for efficient dissemination in vivo. Our findings suggest that, in *T. gondii*-infected monocytes, Rho activation inhibits extravasation and opposes a BBB Trojan horse seeding mechanism, while upregulating interstitial migration to promote the rapid spread of infected cells within tissues, thus promoting systemic parasite dissemination.

## Results

***T. gondii* infection impaired THP-1 monocyte endothelial adherence and transmigration.** We used hCMEC/D3 brain endothelial

<sup>1</sup>Department of Molecular Microbiology, Washington University School of Medicine, St. Louis, MO, USA. <sup>2</sup>Department of Biochemistry and Molecular Biophysics, Washington University School of Medicine, St. Louis, MO, USA. <sup>3</sup>Department of Medicine, Division of Infectious Diseases, Washington University School of Medicine, St. Louis, MO, USA. <sup>4</sup>Present address: York Biomedical Research Institute, Department of Biology, University of York, York, UK. \*e-mail: [sibley@wustl.edu](mailto:sibley@wustl.edu)

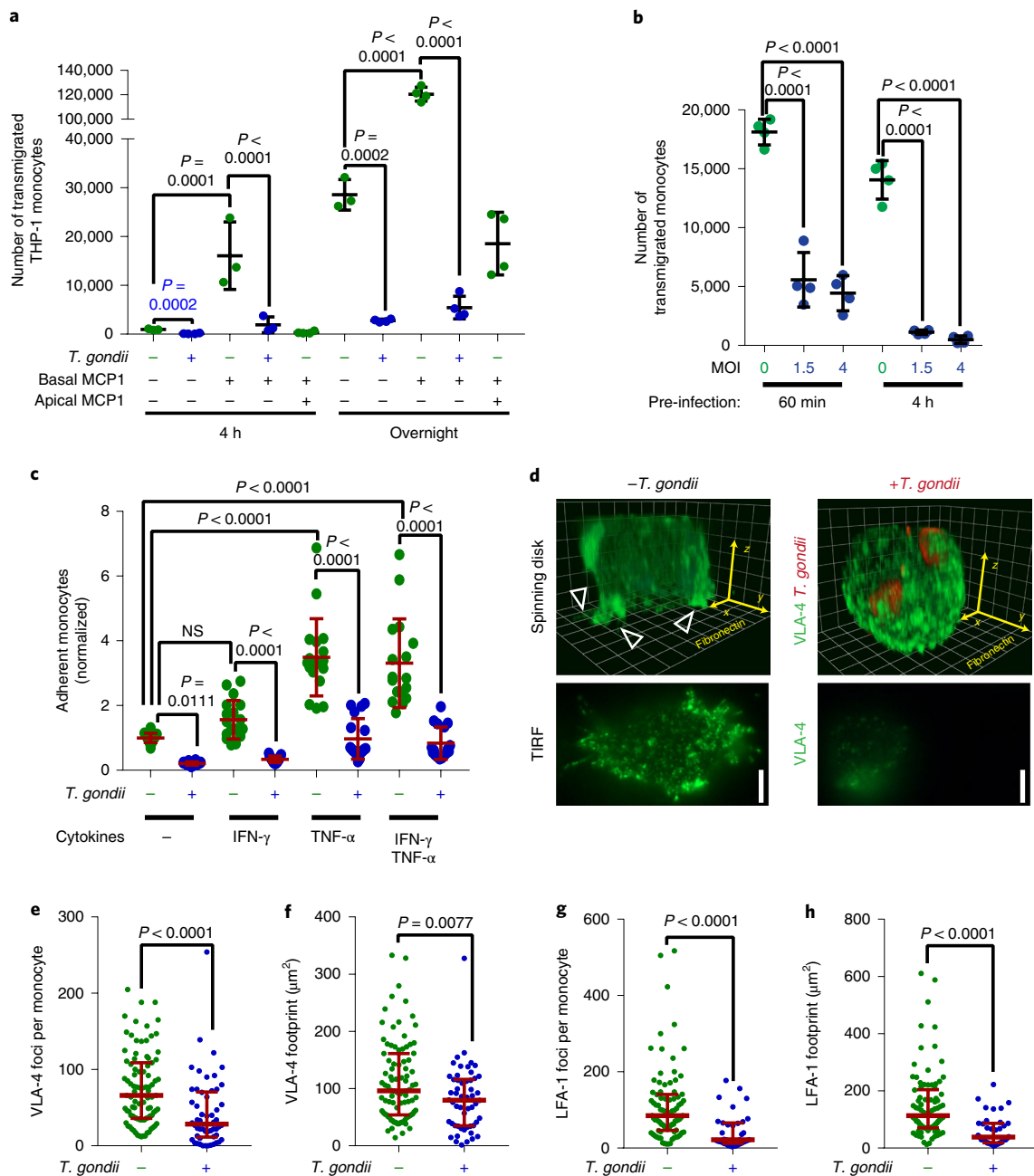


**Fig. 1 | TEM and adherence of infected THP-1 and primary monocytes.** **a, b**, Transmigration of THP-1 monocytes (**a**) and primary human monocytes (**b**) through a hCMEC/D3 BBB model, comparing infected cells (80–95% infected) to mock-treated controls. The chemokine MCP1 was added at  $100 \text{ ng ml}^{-1}$  as indicated. Prior to transmigration, monocytes were pre-infected with ME49-mCherry parasites. Data are shown from one experiment representative of two independent experiments with the same outcome. Each symbol indicates a within-experiment replicate biological sample ( $n=3-4$  per experiment). The lines and error bars denote mean  $\pm$  s.d., respectively. Multiplicity-adjusted  $P$  values from one-way ANOVA and Holm-Sidak's multiple comparison tests are shown in black; two-tailed  $P$  values from unpaired  $t$ -tests are shown in blue. **c**, The number of THP-1 monocytes adhered to hCMEC/D3 monolayers, comparing infected THP-1 (80–95% infected) to mock-treated controls. Data were derived from three independent experiments, each with 5–6 within-experiment replicate biological samples. All quantities were normalized to the mean number of adhered uninfected cells. The lines and error bars indicate mean  $\pm$  s.e.m., respectively. Multiplicity-adjusted  $P$  values from Holm-Sidak's multiple comparison tests are shown (not significant (NS),  $P > 0.05$ ). **d–h**, THP-1 monocytes adhering to fibronectin-coated glass were stained with antibodies against VLA-4 (mAb 9F10) and LFA-1 (mAb TS2/4). In **d**, 3D renderings from spinning disc confocal imaging (top) of VLA-4-stained mock (left) and infected (right) THP-1 monocytes, and sample TIRF microscopy images (bottom) of the same cells are shown. The white arrowheads indicate spreading protrusions on the fibronectin surface. Scale bars,  $5 \mu\text{m}$ . Quantification of the number of integrin foci detected in TIRF images per THP-1 cell (**e, g**) and the total integrin-contact-containing surface area occupied by individual cells in TIRF images (**f, h**). Each data point shows an individual monocyte (VLA-4 uninfected,  $n=89$  THP-1 cells; VLA-4 infected,  $n=52$  THP-1 cells; LFA-1 uninfected,  $n=85$  THP-1 cells; LFA-1 infected,  $n=36$  THP-1 cells). The line indicates the median and the error bars represent the interquartile ranges. Infected THP-1 cells were visually confirmed to contain intracellular parasites and compared with mock-treated control THP-1. Data were pooled from three independent experiments. Two-tailed  $P$  values from unpaired Mann-Whitney tests are shown.

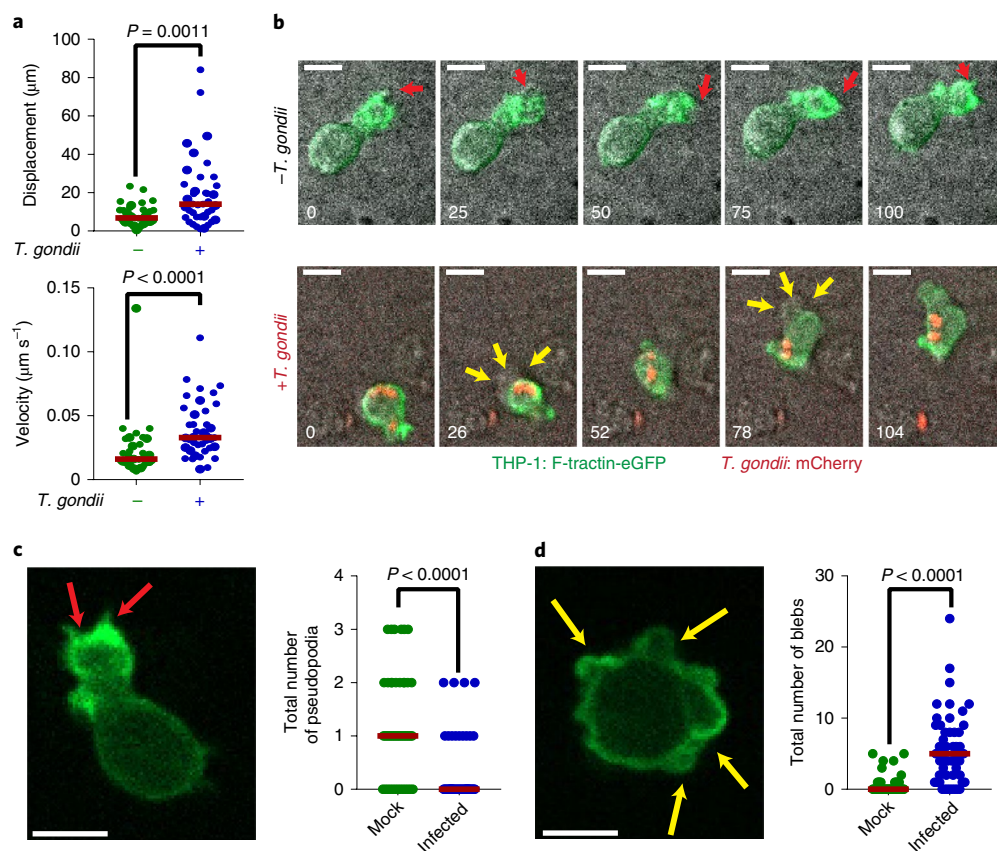


**Fig. 2 | Locomotion of infected THP-1 monocytes on the hCMEC/D3 model of the BBB.** **a**, Displacement (top) and the mean velocity (bottom) of THP-1 monocytes moving over hCMEC/D3 endothelial monolayers, as quantified from 45 min time-lapse microscopy videos. Data from three independent experiments were pooled ( $n=8$ , 10 and 15 examples for mock-treated THP-1 monocytes;  $n=12$ , 12 and 15 examples for infected monocytes), with manually confirmed infected THP-1 compared with mock-treated controls. **b**, Time-lapse images of crawling mock-infected (top) and *T. gondii*-infected (bottom) THP-1 monocytes expressing F-tractin-eGFP. The red arrows indicate F-actin-rich pseudopodia. The yellow arrows indicate membrane swellings that are not enriched for F-actin. The images correspond to Supplementary Videos 1 and 2. The numbers indicate the time in seconds. **c,d**, The number of structures consistent with pseudopodia (**c**) and blebs (**d**) formed by THP-1 monocytes during 5 min periods on hCMEC/D3 (mock,  $n=46$  THP-1 cells; infected,  $n=51$  THP-1 cells). The images show representative pseudopodia (red arrows) and blebs (yellow arrows) and correspond to Supplementary Videos 1 and 3. Data from three independent experiments were pooled. The data points in **a,c,d** denote individual cells and the lines indicate median values. Two-tailed  $P$  values from unpaired Mann-Whitney tests are shown. Scale bars,  $10\ \mu\text{m}$  (**b-d**).

cells cultured on transwell inserts<sup>21</sup> to model TEM across the BBB. Uninfected THP-1 monocytes exhibited time-dependent TEM across hCMEC/D3 monolayers and enhanced migration in response to a chemotactic monocyte chemoattractant protein 1 (MCP1; also known as CCL2) gradient (Fig. 1a). Strikingly, *T. gondii* pre-infection inhibited spontaneous and chemotaxis-driven TEM through hCMEC/D3 monolayers (Fig. 1a). We extended these studies to primary human monocytes and found that TEM was inhibited by previous *T. gondii* infection, at multiple time points (1 h versus 4 h) and infection densities (multiplicity of infection (MOI) of 1.5 versus 4) (Fig. 1b). We further established that parasite inhibition of TEM was observed with primary and immortalized endothelial cells derived from multiple tissues, a hCMEC/D3–astrocyte co-culture system that more faithfully models the BBB<sup>21</sup>, and parasite strains representing all major North American lineages and a highly genetically divergent South American isolate (Supplementary Fig. 1). Notably, the very low basal migration of THP-1 monocytes through HUVECs (Supplementary Fig. 1) may explain why an earlier study failed to detect parasite-induced inhibition of TEM<sup>12</sup>.

We hypothesized that the failure of parasitized monocytes to transmigrate may stem from defects in integrin-mediated adherence and tested this by measuring adherence to hCMEC/D3 monolayers.

As expected, pre-activation of hCMEC/D3 with the inflammatory cytokines tumour necrosis factor- $\alpha$  (TNF- $\alpha$ ) and interferon- $\gamma$  (IFN- $\gamma$ ) enhanced THP-1 monocyte adherence (Fig. 1c). By contrast, infection inhibited adherence to resting and cytokine-activated hCMEC/D3 monolayers (Fig. 1c). We next asked whether this inhibition derived from defects in affinity or avidity enhancement of integrin-mediated adherence<sup>22</sup>. We used total internal reflection fluorescence (TIRF) microscopy to assess avidity-enhancing integrin mobilization in THP-1 monocytes adhering to fibronectin ligands. TIRF imaging revealed that infected cells fail to spread on fibronectin-coated surfaces (Supplementary Fig. 2), forming significantly smaller surface footprints and fewer detectable foci of the integrins LFA-1 and VLA-4 at or just above the fibronectin-coated surface than mock-treated controls (Fig. 1d–h). Flow cytometric analysis of suspension THP-1 monocytes established that infection did not alter surface expression levels of LFA-1 or VLA-4, or MnCl<sub>2</sub>-induced integrin unfolding into high-affinity conformations (Supplementary Fig. 2). Consistent with this finding, the surface integrins of THP-1 monocytes adhering to fibronectin stained positively with an antibody against high-affinity  $\beta_1$  integrin (Supplementary Fig. 2).

Collectively, these results suggest that defects in avidity-enhancing integrin mobilization lead to inefficient adherence of infected

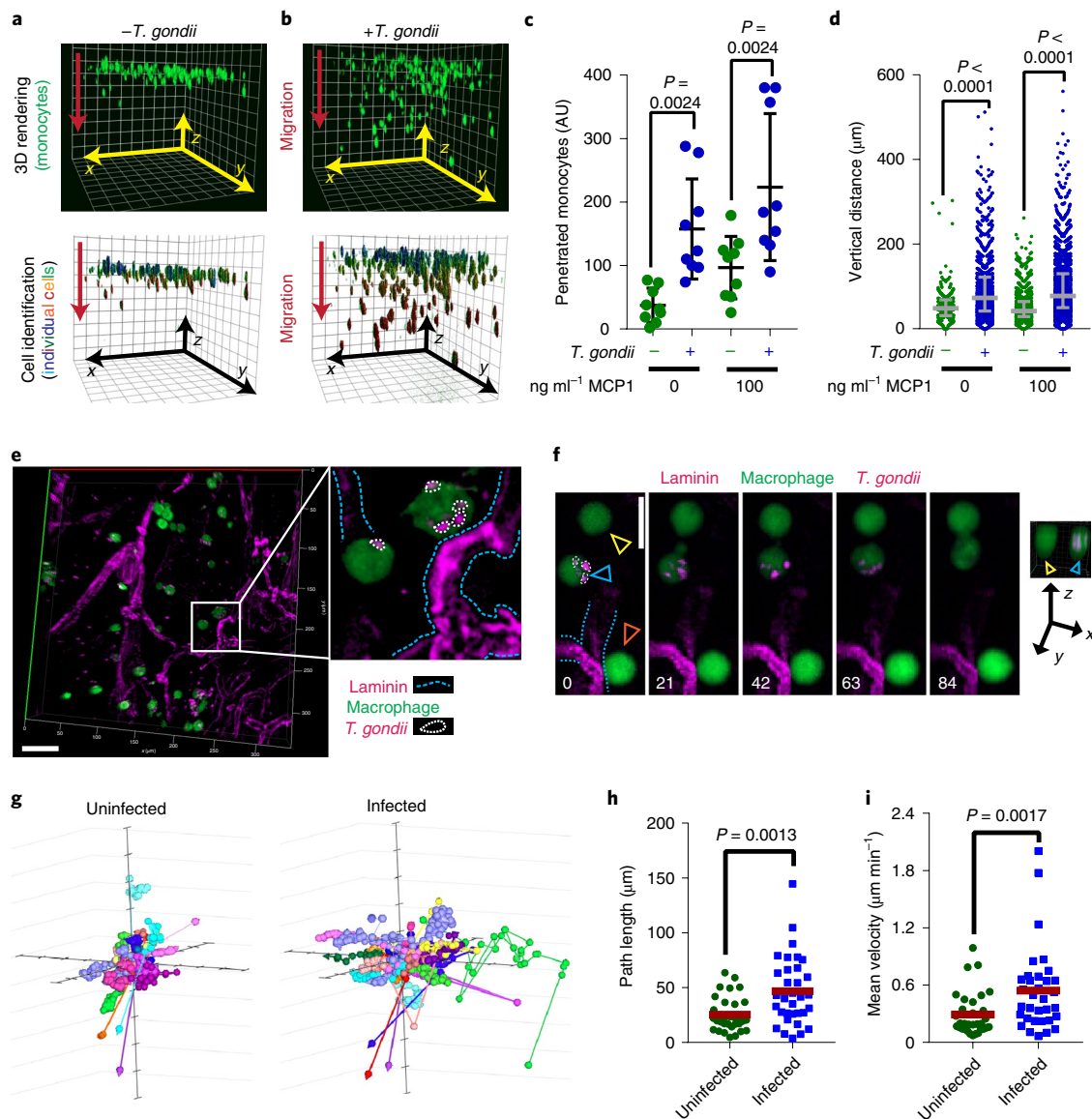


**Fig. 3 | Migration of infected cells through 3D collagen matrices and skin tissue. a, b,** Assay schematic, comparing mock-treated (**a**) and infected (**b**) THP-1 monocytes (infection rate: 80–95%). The top images show 3D renderings created from spinning disk confocal images of THP-1 monocytes captured within collagen matrices. The red arrows indicate the direction of migration. The bottom images show individual cells located by automated protocol. **c, d,** The number of penetrant cells (**c**) and the vertical distance of each cell relative to the matrix top (**d**) were quantified after overnight migration. The plots show pooled data from three independent experiments, each with three technical replicates. **e,** 3D rendering of the dermal ear sheet with vessels (magenta) stained for laminin. RAW macrophages were visualized by GFP; *T. gondii* were visualized by mCherry. Scale bar, 50  $\mu\text{m}$ . Inset: vessels traced in blue and intracellular parasites in white. **f,** Time-lapse series showing a migrating infected cell, with ear dermis vessels traced in blue and intracellular parasites traced in white. The blue arrowheads indicate infected cells; the yellow and orange arrowheads indicate uninfected cells. Scale bar, 20  $\mu\text{m}$ . Right inset: 3D rendering cross-section demonstrating the absence and presence of intracellular parasites in the cells. The numbers indicate the time in seconds. **g,** Displacement plots of RAW macrophage trajectories through the ear dermis tracked over a 2 h period, comparing uninfected and infected RAW macrophages manually identified from pools of ~50% infected cells. **h, i,** The total path length travelled (**h**) and the average velocity (**i**) for each RAW cell in the displacement plots. Data were pooled from three independent experiments for a total  $n = 33$  tracked RAW cells for both uninfected and infected cells. For all analyses, multiplicity-adjusted  $P$  values are shown. Normally distributed data were analysed with one-way ANOVA and Holm-Sidak's multiple comparison post-test and are plotted as mean  $\pm$  s.d. (**c**). Non-normally distributed data were analysed with a Kruskal-Wallis test and a Dunn's multiple comparison post-test and are plotted with medians (lines) (**h, i**) and interquartile ranges (error bars) (**d**).

monocytes to our model BBB, resulting in subsequent failure to transmigrate through the endothelium.

**Parasitized THP-1 monocytes migrated with amoeboid morphology.** We next asked whether, despite their defects in integrin-mediated adherence, infected monocytes could effectively crawl on

model BBB, as was reported with HUVECs<sup>12</sup>. To analyse migration, we cultured hCMEC/D3 cells on a soft polyacrylamide substrate that enhances endothelial maturation<sup>23</sup> and observed the locomotion of THP-1 monocytes expressing the actin polymerization reporter F-tractin-enhanced green fluorescent protein (eGFP) by video microscopy<sup>24</sup>. We found that infection enhanced THP-1 monocyte

migration velocity and displacement across hCMEC/D3 cells (Fig. 2a). Intriguingly, the morphology of infected THP-1 monocytes migrating on hCMEC/D3 cell monolayers markedly differed from mock-treated cells (Fig. 2b–d and Supplementary Videos 1–3). As expected for cells crawling on the endothelium, mock-treated cells moved by forming pointed pseudopodial structures at their leading edge that were enriched in F-actin (Fig. 2b,c, red arrows, and Supplementary Video 1). By contrast, infected cells rarely formed pseudopodial extensions, instead moving in an amoeboid manner typified by a rounded and flowing morphology featuring frequent spherical membrane protrusions (Fig. 2b, yellow arrows, and Supplementary Video 2). A pronounced F-actin-rich leading edge was typically absent in migrating infected cells, and their membrane protrusions instead appeared to be stabilized by F-actin recruitment post-formation (Fig. 2b,d and Supplementary Videos 2 and 3), consistent with the dynamics of bleb-based motility<sup>25</sup>. We quantified the number of structures consistent with pseudopodia (defined by pointed morphology) or blebs (defined by rounded morphology and delayed F-actin recruitment) formed during migration (Fig. 2c,d). Infected cells formed significantly fewer pseudopodia and more blebs than mock-treated controls (Fig. 2c,d).

In summary, although infected THP-1 monocytes migrated efficiently over hCMEC/D3 endothelial cells, their morphology was inconsistent with canonical adhesion-based vascular crawling and instead reminiscent of reports of amoeboid or bleb-driven motility<sup>25,26</sup>.

***T. gondii* infection enhanced monocyte migration through collagen-rich tissues.** The amoeboid morphology of migrating parasitized THP-1 monocytes led us to hypothesize that the parasite may be activating a motility mode similar to integrin-independent leukocyte migration through tissue interstitium<sup>26</sup>. We tested this possibility using a simple migration assay<sup>27</sup> in which cells migrate through three-dimensional (3D) matrices of polymerized collagen I, the primary component of tissue interstitium<sup>28</sup>. We generated 3D renderings from Z-stack images of fluorescently labelled THP-1 monocytes captured after migration into the matrix (Fig. 3a,b, top), and used automated cell identification to quantify the number of monocytes that penetrated into the matrix and their relative vertical positions (Fig. 3a,b, bottom). Infection increased the number of THP-1 monocytes that penetrated into collagen matrices and the distance they migrated (Fig. 3a–d). Enhanced migration was observed whether 3D migration was spontaneous or chemokinetically stimulated with the chemokine MCP1 (Fig. 3c,d). Infection also enhanced the migration of primary human monocytes (Supplementary Fig. 3), confirming the robustness of this phenotype. Because monocytes typically differentiate into phagocytes on

entering tissues, we asked whether infection enhanced macrophage migration in this system and again found that infection enhanced the migration of RAW 264.7 macrophages and murine bone marrow-derived macrophages (BMDMs) (Supplementary Fig. 3).

To better reflect the complex composition and architecture of tissue interstitium, we then adapted a method developed to analyse leukocyte migration through dermal ear sheets<sup>26,29</sup>. We labelled the vessels in the interstitium of ex vivo murine ear dermis by laminin staining and then collected time-lapse microscopy images of RAW 264.7 macrophages crawling within the dermis (Fig. 3e,f). As in the collagen I matrices, infection stimulated migration within the ear dermis, significantly increasing both the distanced travelled and the velocity of migrating RAW macrophages (Fig. 3g,h). Taken together, our results show that *T. gondii* infection enhances macrophage migration in collagen-rich tissue substrates.

**Migration of infected cells relies on host Rho–ROCK and parasite ROP17.** Having determined that *T. gondii*-infected monocytes fail to efficiently traverse endothelial barriers yet robustly migrate through collagen-rich tissues, we next investigated the mechanism by which infection specifically enhances tissue migration.

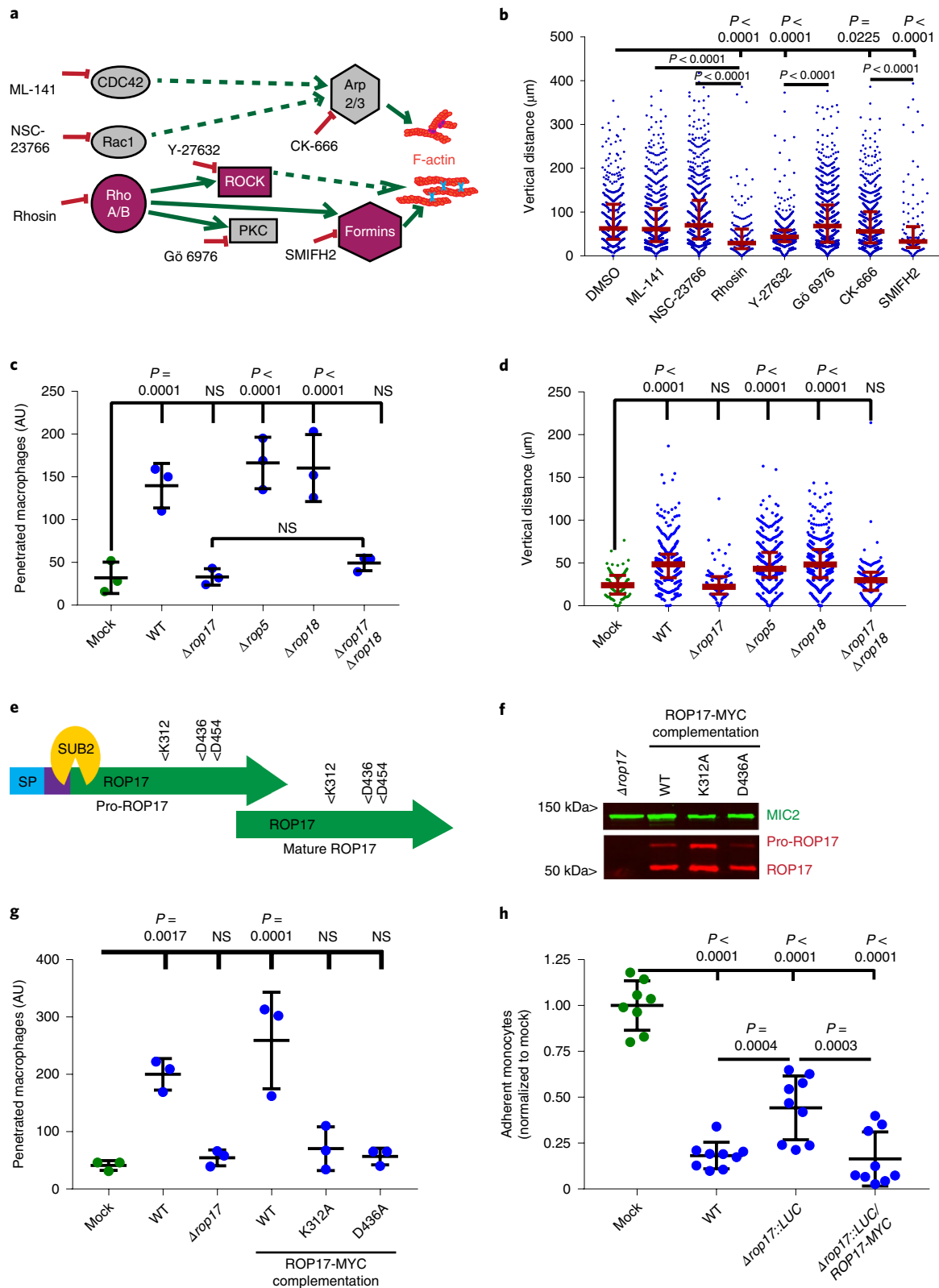
Monocytes and macrophages can migrate through 3D substrates via distinct modes that differ in their dependence on integrins: Rho-dependent amoeboid movement based on actomyosin contractility; and Rac-dependent mesenchymal crawling based on branched actin protrusion<sup>30–32</sup>. We used the compounds ML-141, NSC-23766 and Rhosin to disrupt CDC42, Rac and Rho signalling<sup>33</sup> (Fig. 4a) and found that only inhibition of Rho decreased the migration of parasitized THP-1 monocytes (Fig. 4b). We further found that inhibition of the Rho effector ROCK with the compound Y-27632 significantly decreased the distance travelled by parasitized THP-1 monocytes (Fig. 4b). By contrast, inhibition of the Rho effector protein kinase C- $\alpha$  with the compound Gö 6976 (ref. <sup>34</sup>) had a minimal effect on migration (Fig. 4b). Rho–ROCK signalling often leads to motility via formin-mediated actin polymerization. Supporting the relevance of Rho and ROCK in our system, we found that SMIFH2 inhibition of formins<sup>35</sup> had a significantly larger dampening effect on the migration of infected THP-1 monocytes than did CK-666 (ref. <sup>36</sup>) inhibition of the branched actin nucleator Arp2/3 (Fig. 4b). Migration of infected RAW 264.7 macrophages and murine BMDMs was also blocked by Y-27632 ROCK inhibition (Supplementary Fig. 3), suggesting a shared mechanism of enhanced migration in human monocytes and murine macrophages.

We next tested whether infection also enhanced mesenchymal migration through Matrigel. Infection did not robustly enhance migration through dense Matrigel (Supplementary Fig. 3). However, a protease inhibitor cocktail that suppresses mesenchymal

**Fig. 4 | Enhanced tissue migration may involve Rho–ROCK and requires parasite ROP17.** **a**, Rho GTPase signalling and inhibitors. Dashed arrows indicate indirect interactions; solid arrows indicate direct interactions. PKC, protein kinase C. **b**, Distance migrated by infected THP-1 monocytes (infection rate of 80–95%, compared with mock-treated controls) into 0.8 mg ml<sup>-1</sup> collagen I matrix loaded with 100 ng ml<sup>-1</sup> MCP1, during inhibitor treatment (10  $\mu$ M ML-141, 100  $\mu$ M NSC-23766, 100  $\mu$ M Rhosin, 30  $\mu$ M Y-27632, 1  $\mu$ M Gö 6976, 100  $\mu$ M CK-666 and 30  $\mu$ M SMIFH2). **c,d**, Migration of RAW 264.7 macrophages in 2 mg ml<sup>-1</sup> collagen matrices after pre-infection with parasites of the indicated genotype (infection rate of ~90%, compared with mock-treated controls). The number of penetrated cells (**c**) and the distance travelled (**d**) are shown. **e**, A schematic of the ROP17 protein, indicating catalytic triad residues and a putative SUB2 processing site. The purple region indicates the location at which the 5'-peptide is removed by SUB2. SP, signal peptide. **f**, Western blot of samples from parasites of the indicated genotype and probed with antibodies against MYC and *T. gondii* MIC2. The blot is representative of two independent experiments. **g**, The number of RAW macrophages migrated into a 2 mg ml<sup>-1</sup> collagen matrix after pre-infection with *T. gondii* of the indicated genotype (infection rate of ~90%). **h**, Adherence of THP-1 monocytes to IFN- $\gamma$  or TNF- $\alpha$  (200 U ml<sup>-1</sup>) stimulated hCMEC/D3 endothelial monolayers, comparing *T. gondii* pre-infection with the indicated genotypes (infection rate of 80–95%) to mock-treated controls. Pooled data from three independent assays are shown, each with three within-experiment biological replicate samples. The plots were normalized to the mean number of adherent mock-infected THP-1 monocytes in each experiment. The plots in **b–d,g** show data from one experiment representative of three independent assays, each with the same outcome and three replicate biological samples. The black lines and error bars indicate mean  $\pm$  s.d., respectively (**c,g,h**), and the red lines and error bars indicate the median and interquartile range, respectively (**b,d**). Statistical significance was assessed with one-way ANOVA and Holm–Sidak's multiple comparison test for normally distributed data (**c,g,h**), and Kruskal–Wallis test and Dunn's multiple comparison test for non-normal distributions (**b,d**). For all analyses, multiplicity-adjusted *P* values are shown (NS, *P* > 0.05).

migration<sup>31</sup> subtly decreased the number of infected macrophages that successfully migrated into the Matrigel matrix (Supplementary Fig. 3). These results suggest that, while infection does not suppress macrophage mesenchymal migration, parasite-enhanced migration primarily activates an integrin-independent and Rho-ROCK-dependent amoeboid migratory mode.

The ability of Rho inhibition to block migration of infected cells implies that *T. gondii* enhances motility by acting at or upstream of Rho. *T. gondii* secretes an array of effector proteins into host cells, several of which interfere with innate immunity<sup>37,38</sup>. None of these effectors is known to target the host cytoskeleton, and the *T. gondii* genome does not encode obvious analogues to Rho



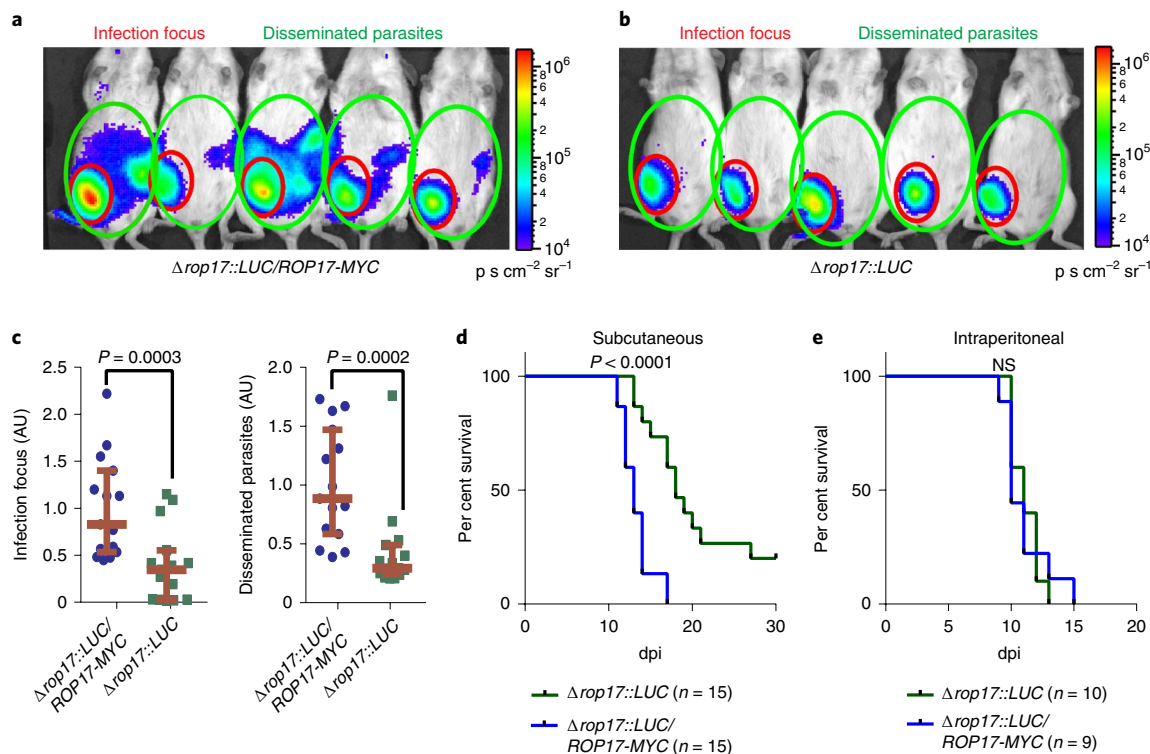


**Fig. 5 | Role of ROP17 during in vivo infection.** **a–e**, Female CD1 mice were infected subcutaneously (**a–d**) or intraperitoneally (**e**) with 200 *T. gondii* of the indicated genotype. Parasite burden and spread were monitored by intravital luminescence imaging before fatality (**a,b**, 8 d post-infection (dpi)), and survival was monitored daily (**d,e**). The parasite luminescence signal in the infection focus was subtracted from the total parasite signal in individual mice to quantify parasites disseminated beyond the infection nidus; representative images and quantification regions are shown (**a,b**). Pooled data from three independent subcutaneous infections (5 mice per group) and two independent intraperitoneal infections (4–5 mice per group) are shown as the total normalized luminescence signal in individual mice (**c**, left: infection nidus; right: dissemination region) with median values and interquartile ranges indicated, and survival curves (**d,e**). Luminescence data were analysed by a two-tailed Mann–Whitney test, and mouse survival was analysed by a Gehan–Breslow–Wilcoxon test (NS,  $P > 0.05$ , one tailed).

guanine nucleotide exchange factors (GEFs) or GTPase-activating proteins (<http://toxodb.org>). However, we hypothesized that the secreted *T. gondii* protein kinases ROP17 and ROP18, which we previously showed to phosphorylate immunity-related GTPases (IRGs)<sup>39</sup>, might also interact with Rho GTPases, perhaps acting by targeting one of several previously identified phospho-activated Rho GEFs<sup>40</sup>.

We infected RAW 264.7 macrophages with  $\Delta rop5$ ,  $\Delta rop17$  and  $\Delta rop18$  parasites and determined that only *ROP17* was required for enhanced penetration into and travel through collagen (Fig. 4c,d), with  $\Delta rop5$  and  $\Delta rop18$  parasites enhancing migration as effectively as wild-type (WT) parasites (Fig. 4c,d). No synergy with ROP18 was evident, as  $\Delta rop17\Delta rop18$  parasites blocked migration no more effectively than  $\Delta rop17$  parasites (Fig. 4c,d). ROP17 shows kinase activity in vitro<sup>39</sup>, but the functional relevance of this kinase activity remains untested. The ROP17 catalytic triad is conserved and easily identifiable<sup>41</sup> (Fig. 4e). We generated  $\Delta rop17$  parasites complemented with either a MYC-tagged WT *ROP17* allele or mutant alleles in which disruption of single catalytic triad residues (K312A and D436A) should ablate kinase activity. *ROP17*<sup>WT</sup>-MYC, *ROP17*<sup>K312A</sup>-MYC and *ROP17*<sup>D436A</sup>-MYC were all expressed at similar levels and accumulated as immature pro-proteins and a mature processed variant (Fig. 4f). Complementation of  $\Delta rop17$  with *ROP17*<sup>WT</sup>-MYC restored collagen migration, whereas both catalytic triad mutants phenocopied  $\Delta rop17$  (Fig. 4g), demonstrating that ROP17 kinase activity is required for enhanced migration.

If ROP17 functions by activating Rho signalling, this could also lead to inhibition of Rac-dependent processes, such as endothelial

adherence and transmigration via Rho–Rac crosstalk<sup>42</sup>. Accordingly, we tested whether ROP17 is involved in parasite inhibition of monocyte adherence to our hCMEC/D3 model BBB. Parasites lacking *ROP17* inhibited the adherence of THP-1 monocytes, although the observed decrease was less dramatic than WT parasites (Fig. 4h). This result suggests that, while ROP17 contributes to parasite inhibition of endothelial adherence, another effector is required for complete suppression, in contrast to the essential role of ROP17 in enhanced migration through collagen-rich 3D substrates.

**ROP17 ablation slows parasite dissemination and eliminates enhanced tissue migration of infected monocytes in vivo.** We then asked whether ROP17-dependent enhancement of monocyte tissue migration alters parasite dissemination in the murine model. We used intravital bioluminescence imaging to observe parasite dissemination after challenge with luciferase-expressing parasites. In mice infected subcutaneously with knockout ( $\Delta rop17::LUC$ ) versus complemented ( $\Delta rop17::LUC/ROP17-MYC$ ) parasites, we found that ROP17-deficient parasites expanded less at the injection site and spread more slowly, resulting in lower parasite burdens inside and outside of the infection nidus (Fig. 5a–c). Although partial, this reduced dissemination led to a significant enhancement in mouse survival (Fig. 5d).

Previous studies have theorized roles for ROP17 in promoting optimal in vitro growth in type II *T. gondii*<sup>43</sup> and in synergizing with ROP18 in defending the parasitophorous vacuole from IFN- $\gamma$ -activated host IRGs<sup>39</sup>. We accordingly asked whether the delayed in vivo dissemination of our type I  $\Delta rop17::LUC$  parasites

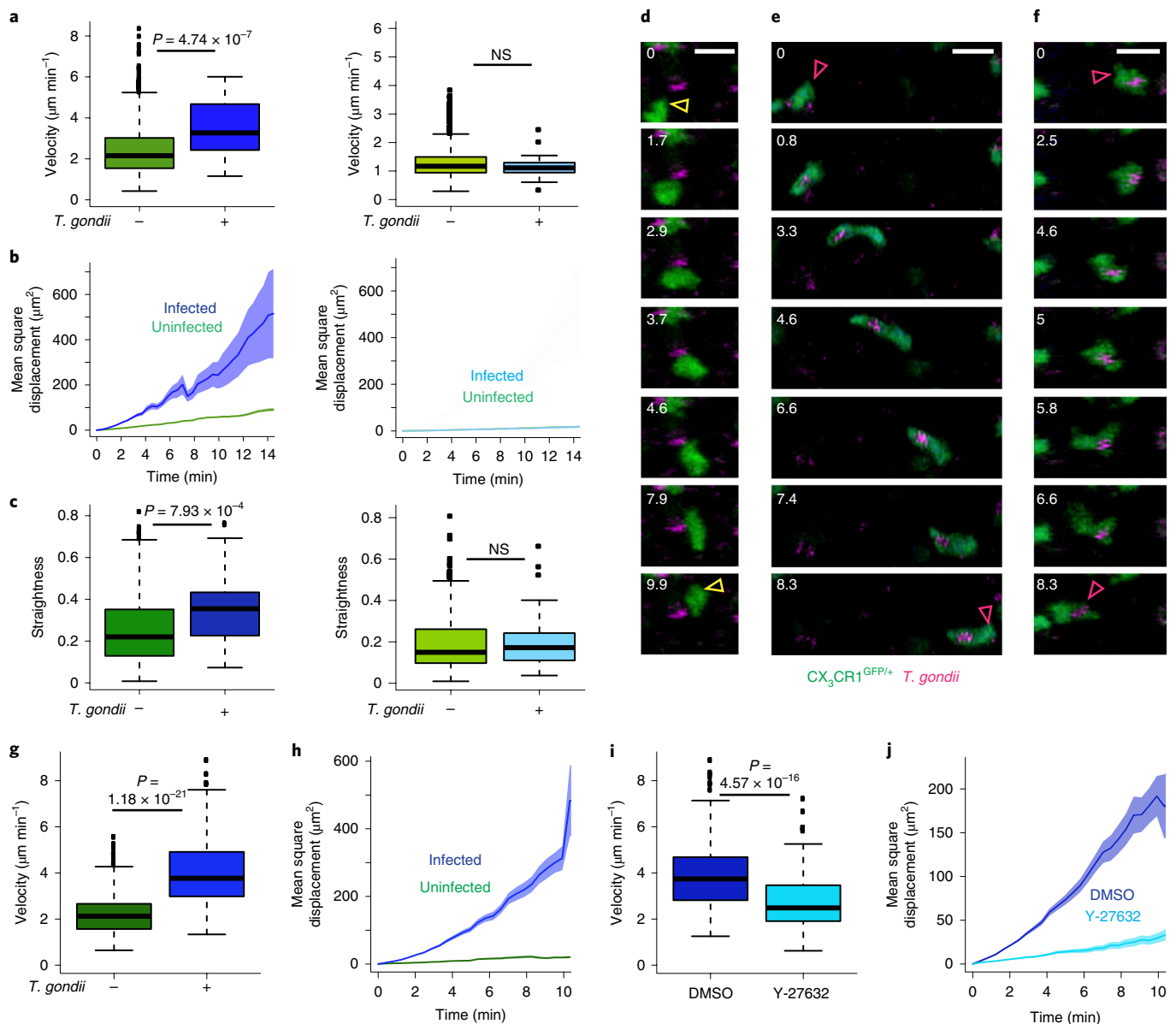


**Fig. 6 | In vivo and ex vivo motility of splenic  $\text{CX}_3\text{CR1}^{\text{GFP/+}}$  cells infected with WT and  $\Delta\text{rop17}$  parasites. a–f**, Intravital two-photon spleen imaging was performed 2–4 h after infecting  $\text{CX}_3\text{CR1}^{\text{GFP/+}}$  mice intravenously with  $2\text{--}4 \times 10^7$  WT or  $\Delta\text{rop17}$  parasites labelled with Cell Tracker Red CMPTX. Track speed (**a**) and mean square displacement (**b**) of all tracked cells as well as the median track straightness of the motile subset (**c**) are plotted, comparing infected and uninfected cells from the same videos (left: WT *T. gondii* infections, infected  $n = 34$ , uninfected  $n = 1,783$ ; right:  $\Delta\text{rop17}$  infections, infected  $n = 42$ , uninfected  $n = 1,228$ ). Time-lapse series of migrating cells displaying typical morphology are also shown (**d–f**). The start and end positions of migrating monocytes are indicated by the yellow arrowheads (uninfected, **d**) and the pink arrowheads (infected, **e, f**). Scale bars,  $10 \mu\text{m}$ . The numbers indicate the time in minutes. The images in **d–f** correspond to Supplementary Videos 4–6. **g–j**, Two-photon imaging was performed after infecting ex vivo spleen sections for 60 min with WT Cell Tracker Red CMPTX-labelled *T. gondii* (tracked  $n = 108$ ) or buffer control (tracked  $n = 148$ ). Spleen sections were infected ex vivo and imaged during superfusion with  $30 \mu\text{M}$  Y-27632 (tracked  $n = 225$ ) or the equivalent volume of dimethylsulfoxide (DMSO; tracked  $n = 175$ ) (**i, j**). Median track speed (**g, i**) and mean square displacement (**h, j**) of tracked  $\text{CX}_3\text{CR1}^{\text{GFP/+}}$  monocytes are plotted. Data were pooled from multiple videos captured during three (**a–c, i, j**) or one (**g, h**) independent experiment(s). The shaded areas indicate the s.e.m. for mean square displacement (**b, h, j**). In the box plots, the box is the interquartile range, the solid band in the box is the median, the error bars are the minimum and maximum values and the outliers are indicated as dots for track speed (**a, g, i**) and straightness (**c**) plots. Data were analysed by two-tailed Wilcoxon tests (NS,  $P > 0.05$ ).

could derive from deficiencies in intrinsic growth or resistance to IRG-mediated macrophage clearance. To test for inefficient parasite growth in vivo, we challenged mice intraperitoneally with *T. gondii*. Intraperitoneal infection challenges parasites with a robust immune response, whereas passive dissemination via drainage from the peritoneal cavity probably negates motility differences. Hence, intraperitoneal infection should reveal mutants with specific defects in

intrinsic growth or enhanced clearance susceptibility. After intraperitoneal challenge, we observed no difference in the virulence of knockout and complemented  $\Delta\text{rop17}::\text{LUC}$  parasites (Fig. 5e). Likewise, in vitro assays established that  $\Delta\text{rop17}::\text{LUC}$  parasites did not exhibit significant differences in mean plaque number or size when propagated in fibroblasts and compared with complemented  $\Delta\text{rop17}::\text{LUC}/\text{ROP17-MYC}$  parasites, and formed parasitophorous

vacuoles of normal morphology and quantity when parasites were grown in IFN- $\gamma$ -lipopolysaccharide-activated RAW 264.7 murine macrophages (Supplementary Fig. 4). These findings suggest that the in vivo attenuation of  $\Delta rop17::LUC$  parasites is specifically caused by deficient dissemination.

Finally, we used two-photon imaging to assess whether ROP17 was critical for parasites to enhance monocyte tissue migration in vivo. We focused on the spleen as it is readily infected during natural *T. gondii* infections<sup>11</sup> and is the major tissue reservoir of murine monocytes<sup>44</sup>. We first tested whether we could detect monocytes by intravital two-photon spleen imaging in CX<sub>3</sub>CR1<sup>GFP/+</sup> mice, in which the vast majority of splenic CX<sub>3</sub>CR1<sup>+</sup> cells are monocytes or lineage descendants<sup>44</sup>. We differentiated CX<sub>3</sub>CR1<sup>GFP/+</sup> monocytes and phagocytes by morphology, and successfully identified uninfected and infected CX<sub>3</sub>CR1<sup>GFP/+</sup> cells exhibiting monocyte morphology and staining with the monocyte marker CD115 (Supplementary Fig. 5). This staining pattern is consistent with identity as monocytes or differentiating monocyte-derived phagocytes. We found that WT *T. gondii* infection significantly increased the migration of splenic CX<sub>3</sub>CR1<sup>GFP/+</sup> cells with monocyte morphology, enhancing median track speed, mean square displacement and median track straightness (Fig. 6a–c, left). By contrast,  $\Delta rop17$  infection had no statistically significant effect on the measured motility parameters (Fig. 6a–c, right). Consistent with our observations of motility in the BBB model (Fig. 2), infected CX<sub>3</sub>CR1<sup>GFP/+</sup> cells migrated in vivo with a flowing amoeboid morphology suggestive of integrin-independent interstitial migration (Fig. 6d–f and Supplementary Videos 5 and 6). Next, we used an ex vivo spleen explant model (Fig. 6g,h) to test whether the enhanced migration of CX<sub>3</sub>CR1<sup>GFP/+</sup> cells with monocyte morphology was sensitive to ROCK inhibition, as expected for amoeboid interstitial migration. Treatment with Y-27632 significantly inhibited migration, decreasing median track speed and mean square displacement of infected CX<sub>3</sub>CR1<sup>GFP/+</sup> cells (Fig. 6i–l). Overall, our intravital and ex vivo imaging data support the model that ROP17-dependent enhancement of amoeboid interstitial migration in infected monocytes promotes parasite dissemination through tissues in vivo.

## Discussion

Like several other pathogens, *T. gondii* is proposed to exploit leukocytes as Trojan horses that enable access to the CNS<sup>2</sup>. However, evidence for migration of *T. gondii*-infected monocytes across the BBB currently lacks compelling supporting data. Here, we show that in vitro, *T. gondii* infection profoundly impaired monocyte transmigration across a model BBB and integrin-dependent adherence to the endothelium. By contrast, infection enhanced monocyte and macrophage motility on endothelial cells and interstitial migration through 3D tissues, both in vitro and in vivo. Enhanced tissue migration was sensitive to pharmacological inhibition of Rho–ROCK as is typical of integrin-independent amoeboid interstitial migration. We further identified the secreted parasite kinase ROP17 as essential for *T. gondii* to activate tissue migration. By infecting mice with ROP17-deficient *T. gondii*, we showed that loss of parasite-enhanced monocyte/macrophage tissue migration leads to slower parasite dissemination kinetics and prolonged mouse survival. In summary, we show that *T. gondii* dissemination is promoted by ROP17-dependent activation of interstitial tissue migration in infected monocytes, while integrin-dependent processes that lead to endothelial traversal are suppressed.

Although integrins were once thought to be pivotal players for all leukocyte migratory modes, elegant genetic work in mice has established that integrin-independent migration is possible within tissues<sup>26</sup>. When leukocytes interact with vasculature, integrins function as adhesins that enable stable adherence to endothelial ligands and as critical force transducers that convert retrograde actin polymerization into forward movement<sup>45</sup>. However, the 3D

environments of the tissue interstitial space de-emphasize the importance of adhesion. In such tissue environments, low-affinity interactions with the surrounding matrix and Rho–ROCK-driven actin-based contractility can propel leukocytes forward, even in the absence of integrin functionality<sup>26,45</sup>. Here, we report that *T. gondii* infection of monocytes simultaneously inhibited integrin-dependent processes and activated Rho-dependent tissue motility. The failure of infected monocytes to efficiently perform integrin-mediated adherence or TEM suggests that they are ill-suited to act as Trojan horses that deliver parasites across the BBB. Instead, we speculate that enhanced tissue migration could carry infected monocytes via lymphatic drainage into the circulation, by enhancing rates of either leukocyte entry into lymphatics or travel through lymph nodes and subsequent exit into efferent lymphatics that lead towards the lymphovenous valve. Once in the circulation, parasites may egress from infected monocytes and directly invade the brain endothelium<sup>9</sup>, a process that could perhaps be aided by infected monocytes embolizing in small CNS capillaries.

Our studies demonstrate that *T. gondii* infection programmes monocytes to preferentially migrate through tissues in an amoeboid manner by using the secreted kinase ROP17 to activate Rho–ROCK-dependent processes. During natural infections, *T. gondii* first encounters and infects leukocytes in the intestinal lamina propria<sup>6</sup>. We speculate that *T. gondii* invades lamina propria monocytes or monocyte-derived macrophages early during infection and activates their tissue migration to rapidly escape this compartment. We focused on monocyte and macrophage motility due to the abundance of infected monocytes in the blood during murine infections<sup>11</sup>. In addition, *T. gondii* manipulates dendritic cell motility<sup>17–20</sup>, and dendritic cells are infected in the lamina propria, although, again, less commonly than monocytes and macrophages<sup>6</sup>. The specific leukocyte subsets that are the primary target(s) of ROP17-mediated enhanced tissue migration in vivo remains a question for further study. Consistent with a role in dissemination, we showed that infection enhanced in vivo migration of CX<sub>3</sub>CR1<sup>+</sup> monocytes in the spleen, and that loss of ROP17-dependent enhanced tissue migration delayed the dissemination of hypervirulent type I *T. gondii*. Similarly, *ROP17* ablation was reported to cause a near complete loss of brain cyst formation in cyst-competent type II *T. gondii*<sup>43</sup>, probably as a consequence of reduced dissemination.

Our findings establish that the catalytic activity of the secreted serine/threonine kinase ROP17 is required for *T. gondii* to enhance macrophage tissue migration. Previous work established that ROP17 forms a complex with the kinase ROP18 and the regulatory pseudokinase ROP5, and synergizes with these partners to ensure parasite survival within activated macrophages by phosphorylating IRGs<sup>39</sup>. In contrast to this IRG defence system, we found that when enhancing tissue migration, ROP17 also functions independently of ROP5 and ROP18. We presume that ROP17 enhances tissue migration by phosphorylating an unknown, non-IRG target, which might directly or indirectly regulate host Rho–ROCK signalling. ROP17 could access cytosolic substrates either when injected into the host cytosol during parasite invasion or following subsequent recruitment to the cytosolic face of the parasitophorous vacuole membrane<sup>39,46</sup>. We previously showed that ROP17 exhibits a strong preference for threonine phosphorylation and a slight preference for surrounding hydrophobic residues<sup>39</sup>. Although kinase targets cannot be easily predicted from substrate preference motifs, the Rho GEFs VAV and GEF-H1, the Rho GTPase-activating protein DLC1 and Rho GDI1 can all be phosphoregulated<sup>40</sup> and are, therefore, candidate substrates through which ROP17 could activate Rho-driven amoeboid migration. Alternatively, ROP17 may facilitate export of a separate effector, given the recent report that it facilitates translocation of dense granule proteins across the parasitophorous vacuole membrane<sup>47</sup>. Future elucidation of ROP17 substrates may provide insights into *T. gondii* dissemination and the mechanisms

that prompt leukocytes to adopt integrin-independent migratory strategies in vivo.

## Methods

**Parasite culture.** *T. gondii* parasites were propagated in human foreskin fibroblasts obtained from the laboratory of J. Boothroyd at Stanford University (Stanford, CA, USA). Type II ME49-mCherry parasites were used throughout in Figs. 1–3 unless otherwise indicated. All studies with ROP17 were performed in a type I RH  $\Delta ku80 \Delta hxpgrt$  background. Source and generation details for all *T. gondii* strains used are described in Supplementary Table 1.

**Primary human monocytes.** Primary human monocytes were obtained by flushing human peripheral blood from leukoreduction (LRS) chambers provided by the Washington University School of Medicine apheresis center, and then isolating monocytes via negative immunodensity selection with a RosetteSep Human Monocyte Enrichment Cocktail (Stem Cell Tech) and Ficoll-Paque sedimentation. To confirm successful isolation of monocytes, cells were analysed for CD33 and CD14 positivity by flow cytometry. Monocytes were cryopreserved immediately after harvest in 7.5% dimethylsulfoxide and 10% human serum. Following thawing, primary monocytes were cultured in RPMI supplemented with 10% human serum, 1% non-essential amino acids, 10 mM HEPES and 100 U ml<sup>-1</sup> penicillin–1 µg ml<sup>-1</sup> streptomycin.

**Culture of cell lines.** The human brain endothelial cell line hCMEC/D3 (ref. 48) was obtained from the laboratory of R. Klein at Washington University and grown as previously described<sup>21</sup> from passages 28 to 34. THP-1 monocytes were cultured in RPMI media supplemented with 10% FBS. RAW 264.7 macrophages were cultured in DMEM media supplemented with 10% FBS. All lines were confirmed as mycoplasma negative with the e-Mycoplasm plus mycoplasma PCR detection kit (Boca Scientific) on acquisition.

**Culture of primary cells.** Primary human aortic endothelial cells (HAECs) at passage three were obtained from Lonza and cultured in fully supplemented EGM-2 media (Lonza). HAECs from passages five to seven were used in experiments. Primary human astrocytes were acquired from ScienCell and cultured in Astrocyte Media (ScienCell) in flasks coated with 2 µg cm<sup>-2</sup> collagen. On receipt, astrocytes were cryopreserved at passage one. Thawed aliquots at passage three or four were used for experiments.

**Growth of hCMEC/D3 on polyacrylamide pads.** To provide a soft substrate for cell growth, 0.4% polyacrylamide pads were prepared in glass-bottom dishes as previously described<sup>23</sup> and then coated with 150 µg ml<sup>-1</sup> rat collagen I. Dishes were each seeded with 5 × 10<sup>4</sup> hCMEC/D3 and grown until confluence. EA.hy926 HUVECs were obtained from the American Type Culture Collection and cultured in DMEM supplemented with 10% FBS.

**Microscopy.** In vitro imaging studies were performed on a Axio Observer Z1 inverted microscope (Zeiss) that features modules for conventional fluorescence, spinning disk confocal and TIRF microscopy. Conventional fluorescence images were acquired with illumination from a Colibri LED light source (Zeiss) and ORCA-ER digital camera (Hamamatsu Photonics). Spinning disk and TIRF images were acquired using illumination from 488-nm and 561-nm solid-state lasers (Zeiss) and Evolve 512 Delta EMCCD cameras (Photometrics). For all modules, Zen software (Zeiss) was used for image acquisition.

**Time-lapse imaging of monocyte crawling on hCMEC/D3 endothelium.** To quantify crawling, THP-1 monocytes were labelled with CellTrace Oregon Green 488 Carboxy-DFFDA (Thermo Fisher), resuspended in Migration RPMI (phenol-free RPMI supplemented with 3% FBS, 1% non-essential amino acids (Gibco) and 10 mM HEPES) and then infected with freshly harvested *T. gondii* at an MOI of ~4.5 for 3–6 h. Just prior to imaging, the hCMEC/D3 dishes were changed to Migration RPMI and then equilibrated for 10 min at 37 °C in the incubation chamber of an inverted microscope. Alternating conventional bright-field and fluorescent images were captured at 1-min intervals over a 45-min period, using the above-described spinning disk microscopy system with a ×40 C-Apochromat water immersion objective (NA 1.20). Automated tracking of individual monocytes' centroids was performed using Velocity software (PerkinElmer). To follow actin polymerization dynamics, cells were transfected with F-tractin-eGFP 1 d before imaging crawling on soft-substrate-supported hCMEC/D3. Actin polymerization videos were collected with the above spinning disc imaging system, using 5-s intervals over 5-min periods. Structures consistent with pseudopodia or blebs were manually counted.

**Animals.** All protocols requiring animals were approved by the Institutional Animal Care and Use Committee at the Washington University in St Louis School of Medicine. Mice were housed in Association for Assessment and Accreditation of Laboratory Animal Care International-approved facilities at Washington University. CX<sub>3</sub>CR1<sup>GFP/+</sup> mice were obtained from Jackson Laboratory or as

generous gifts from G. Randolph (Washington University). CD1 mice were purchased from Charles River Lab.

**Intravital two-photon imaging.** Heterozygous CX<sub>3</sub>CR1<sup>GFP/+</sup> mice were infected with 2–4 × 10<sup>7</sup> Cell Tracker Red CMPTX-labelled *T. gondii* via tail vein injection. To label CD115, 40 µg phycoerythrin-conjugated anti-CD115 was introduced retro-orbitally about 30 min before imaging. Time-lapse imaging was performed with a custom-built 2P microscope<sup>49,50</sup> equipped with a Chameleon Vision II Ti:Sapphire laser (Coherent) and a 1.0 NA ×20 water dipping objective (Olympus). SlideBook software (Intelligent Imaging Solutions) was used to control laser scanning, image acquisition and z-step movements. In vivo imaging of the spleen used a custom imaging chamber built in-house<sup>49</sup>. Mice were anaesthetized with 1.5% isoflurane in carbogen carrier gas and body temperature was maintained with a warming plate. The skin was cut away over the spleen and a small incision was made in the peritoneal membrane to access the spleen. The spleen was lifted gently with forceps and a small portion was secured to thin plastic support with VetBond adhesive. The upper chamber plate was lowered on to the tissue until contact was made with the coverslip and then the upper chamber filled with water for imaging. The plastic support was then clipped to the upper chamber plate with a hair pin to dampen movement artefacts. Small electrical heaters (resistors) attached to both the upper and the lower chamber plates were used to prevent the mouse from becoming hypothermic. After the imaging preparation was completed and before imaging, the spleen was examined under the microscope to confirm that blood flow was robust in sinuses and blood vessels. CX<sub>3</sub>CR1-GFP cell migration was analysed using 3D time-lapse imaging for up to 30 min. Fluorescence was excited at 980 nm and fluorescence emission was detected by photomultiplier tubes simultaneously using 495-nm and 560-nm dichroic filters: blue (<495 nm, SHG collagen), green (495–560 nm, eGFP) and red (>560 nm, CMPTX-Toxo). Auto fluorescence appears as mix of colour (495–600 nm) and thus can be discriminated from eGFP and CMPTX. For time-lapse imaging, we acquired a 500 × 500 × 60 µm volume as 31 sequential 2-µm z-steps with a time resolution of approximately 25 s per time point and a x,y resolution of 0.585 µm per pixel. Intravital imaging focused on the red pulp at <100 µm below the surface. Multi-dimensional data sets were exported as TIFFs and rendered in 3D using Imaris (Bitplane). Cell tracking and data analysis were performed using Imaris (Bitplane) and Motility Lab (2ptrack.net). CX<sub>3</sub>CR1<sup>+</sup> cells were identified by GFP signal and tracked in 3D with an automated Imaris protocol. Macrophages were manually excluded on the basis of morphology, and infected monocytes were manually identified by signal from the Cell Tracker Red dye. To assess track speed and mean square displacement, infected monocytes were compared with all unambiguously uninfected monocytes with verified accurate tracks from the same videos (RH infected, n = 34; *Drop17* infected, n = 42; uninfected, N > 1,000). Straightness was assessed in only subsets of each population chosen to have similar track durations (RH-infected monocytes, 74%; RH-uninfected monocytes, 42%; *Drop17*-infected monocytes, 95%; and *Drop17*-uninfected monocytes, 66%).

**Ex vivo two-photon imaging.** For ex vivo imaging, spleens were harvested from CX<sub>3</sub>CR1<sup>GFP/+</sup> mice and adhered onto a plastic coverslip with VetBond adhesive. Spleens were sliced lengthwise with a microtome blade and incubated for 60 min with Cell Tracker Red CMPTX-labelled RH  $\Delta ku80 \Delta hxt$  *T. gondii* or buffer control. After gentle rinsing, the explanted spleen sections were then imaged with the above-described two-photon imaging approach while being superfused with DMEM supplemented with either 30 µM Y-27632 or an equivalent volume of dimethylsulfoxide and aerated with carbogen gas (95% oxygen and 5% carbon dioxide). Image processing and analysis were as above.

**In vivo infections and intravital luminescence imaging.** Female CD1 mice (8–10 weeks of age) were challenged intraperitoneally or subcutaneously in the right rear flank with 200 parasites. Luminescence imaging was performed on mice anaesthetized with 2% isoflurane and injected intraperitoneally with D-luciferin (Biosynth AG) (150 mg per kg) with a Xenogen IVIS200 machine. Luminescence data were analysed with Xenogen Living Image software (Caliper Life Sciences). To quantify disseminated parasites, a region of interest of size fixed to the smallest area of parasite signal near the injection site was denoted as the infection focus, and the signal from this area was subtracted from another fixed-size region of interest that encompassed all parasite signal within each mouse.

**BMDMs.** BMDMs were harvested from the femurs of C57/BL6 mice with standard protocols, matured in BMDM Harvest Media (DMEM, 10% FBS, 5% horse serum, 40 µM L-glutamine, 100 µg ml<sup>-1</sup> gentamicin and 20% L929-conditioned media) and maintained in BMDM Maintenance Media (DMEM, 10% FBS, 5% horse serum, 40 µM L-glutamine, 100 µg ml<sup>-1</sup> gentamicin and 10% L929-conditioned media).

**Generation of transgenic monocytes and macrophages.** THP-1 monocytes were transfected using the Amaxa 4D Nucleofection system (Lonza) and the cell line SG kit. For each transfection, 1 µg plasmid DNA prepared with a PureLink HiPure Plasmid Midiprep Kit (Invitrogen) was used with 2 × 10<sup>6</sup> THP-1 monocytes. RAW 264.7 macrophages were transfected using Lipofectamine LTX with PLUS Reagent (Thermo Fisher) and 7 µg DNA per plasmid, prepared with a NucleoBond Xtra

Midi EF kit (Macherey-Nagel). To generate a stable GFP-expressing line of RAW 264.7 macrophages, we introduced the plasmids pSB-100 and pSB-Bi-GP, followed by selection with  $5 \mu\text{g ml}^{-1}$  puromycin and maintenance in  $2.5 \mu\text{g ml}^{-1}$  puromycin<sup>31</sup>.

**Flow cytometry analysis of integrin expression and activation.** THP-1 monocytes were infected with *T. gondii* at an MOI of ~4.5 for 3 h or IC buffer in equivalent volume. Monocytes were then pelleted and resuspended in Integrin Activation Buffer (Hanks's balanced salt solution, 1 mM  $\text{Ca}^{2+}$ , 1 mM  $\text{Mg}^{2+}$ , 20 mM HEPES and 0.5% FBS, pH 7.4) and equilibrated at  $37^\circ\text{C}$  for 60 min. To activate integrins, monocytes were treated with 9 mM  $\text{MnCl}_2$  for 5 min at  $37^\circ\text{C}$ , then immediately transferred to ice. Live unpermeabilized cells were stained for integrin expression with primary monoclonal antibodies (mAbs): activated LFA-1, mAb24 (Abcam); activated VLA-4, mAb 12G10 (Abcam); LFA-1, mAb TS2/4 (BioLegend); VLA-4, mAb 9F10 (Biolegend); and Alexa-488-conjugated anti-mouse IgG secondary antibody for detection. After staining, cells were fixed with ice-cold 4% formaldehyde and stored at  $4^\circ\text{C}$  in PBS before analysis with a BD-FacsCanto. Forward and side-scatter gating was used to separate monocytes from debris and extracellular parasites.

**Parasite growth in activated macrophages.** RAW 264.7 macrophages were activated for 18 h with mouse IFN- $\gamma$  ( $10 \text{ U ml}^{-1}$ ) and lipopolysaccharide ( $1 \text{ ng ml}^{-1}$ ), then infected with *T. gondii*. After 24 h, cells were fixed and parasites were stained with anti-DG52 antibody. The number of parasitophorous vacuoles present in five fields per technical replicate was counted. RAW 264.7 macrophages were infected with *T. gondii*. After fixation and permeabilization with 0.05% saponin, cells were stained with anti-GRA7 (ref. <sup>33</sup>).

**Static adherence of monocytes to hCMEC/D3 cells.** Optical grade black 96-well plates were seeded with  $1 \times 10^5$  hCMEC/D3 cells per well and grown to confluence. The day before the adherence assay, hCMEC/D3 cells were activated overnight with IFN- $\gamma$  ( $200 \text{ U ml}^{-1}$ ) and TNF- $\alpha$  ( $200 \text{ U ml}^{-1}$ ) as indicated. THP-1 monocytes were labelled with Cell Trace CFSE (Invitrogen) and then infected with *T. gondii* at an MOI of ~4.5. After 4 h of infection,  $10 \times 10^5$  monocytes per well were transferred to the pre-activated hCMEC/D3 cells and allowed to adhere for 30 min at  $37^\circ\text{C}$ . Non-adherent monocytes were then removed by vigorous rinsing, and the remaining adherent monocytes were fixed with 4% formaldehyde. Samples were imaged with a Cytation 3 imager (Biotek), using automated cell finding from CFSE fluorescence to locate focal planes. Approximately 80% of the well bottom was imaged, and Gen5 software (Biotek) was then used to quantify the number of adherent monocytes. Three independent experiments were performed, each with 5–6 technical replicates per condition.

**Integrin staining and TIRF microscopy.** THP-1 monocytes were pre-infected with *T. gondii* for 4 h (MOI of 4) and then allowed to adhere onto  $50 \mu\text{g ml}^{-1}$  fibronectin-coated glass coverslip dishes (MatTek) for 30 min. Samples were then gently rinsed with PBS and fixed for 10 min with ice-cold 4% formaldehyde in PBS. Cells were permeabilized with 0.05% saponin and stained with mAbs against LFA-1 (TS2/4) or VLA-4 (9F10), followed by Alexa fluorophore-conjugated secondary antibodies. Samples were imaged in PBS with the earlier-described TIRF microscopy system and a  $\times 100$  oil Plan-Apochromat (NA 1.46) objective. Tandem Z-stack series of the same cells were captured with the earlier-described spinning disk system to visualize cells as infected or uninfected. TIRF images were analysed in Volocity software. Cell outlines were manually traced, and integrin foci were identified using the Volocity Spot Finder function.

**TEM assays.** TEM was quantified by allowing CFSE-labelled monocytes to cross in vitro barriers of endothelial cells grown on 24-well format Falcon transwell permeable supports with polyethylene terephthalate membranes and 8- $\mu\text{m}$  pores. To create a flat surface for automated imaging, 15-mm coverslips coated with 0.1% gelatin were placed in the basal chambers. After allowing for transmigration, transwell inserts were removed and basal chambers were fixed with 0.4% formaldehyde. Rectangular grids covering about 90% of the basal chambers were then imaged in medium-throughput format using a Cytation 3 (Biotek) plate imager with  $\times 10$  objective. Gen5 software (Biotek) was used to quantify the number of monocytes in each basal chamber, as defined by size and fluorescence signal. Where indicated, chemotactic gradients were generated by adding  $100 \text{ ng ml}^{-1}$  MCP1 (Peprotech) to basal transwell chambers. The hCMEC/D3 cell line was seeded onto transwell membranes pre-coated with  $150 \mu\text{g ml}^{-1}$  rat collagen I, using  $4 \times 5 \times 10^5$  cells per  $\text{cm}^2$  and grown 5–7 d before TEM assays. Barrier integrity was confirmed by measuring transendothelial electrical resistance (TEER) with an EVOM2 VoltOhmmeter (World Precision Instruments). At the time of the TEM assays, hCMEC/D3 cells typically achieved a TEER of 50–70  $\Omega$  per  $\text{cm}^2$ .

For assays using HAECs and HUVECs, EA.hy926 cells were seeded on  $10 \mu\text{g ml}^{-1}$  fibronectin-coated transwell membranes using  $0.5\text{--}1 \times 10^5$  cells per  $\text{cm}^2$  and cultured for 2 d to generate a robust barrier. Barrier integrity was confirmed by measuring TEER with an EVOM2 VoltOhmmeter (World Precision Instruments). At the time of the TEM assays, HAECs typically achieved a TEER of 40–50  $\Omega$  per  $\text{cm}^2$  and HUVECs typically achieved a TEER of 80–120  $\Omega$  per  $\text{cm}^2$ .

**Mesenchymal migration through Matrigel.** Matrigel ( $8.3 \text{ mg ml}^{-1}$ ) was polymerized in optical-grade black 96-well plates for 45 min at  $37^\circ\text{C}$  and then equilibrated for  $\geq 60$  min in DMEM supplemented with 3% serum. In each well,  $1 \times 10^5$  BMDM pre-labelled with Cell Trace CFSE (Invitrogen) and pre-incubated with *T. gondii* (infection rate of ~75%) or buffer controls, and then were allowed to migrate into the matrix. After overnight migration at  $37^\circ\text{C}$  and 5%  $\text{CO}_2$ , the samples were rinsed with PBS and fixed with 4% formaldehyde. Z-stack image series of the BMDM captured within the collagen matrices were captured with the above-described spinning disk microscopy system and an EC Plan-Neofluar  $\times 10$  (NA 0.30) objective. Volocity software was used to generate 3D renderings of the Z-stacks and locate each macrophage using an automated Object Finding protocol based on fluorescence intensity and cell size. Vertical distance migrated was calculated as the distance between the centroid of the cell with the highest z-position and every other cell. To ensure that analysed macrophages were not superficially adhered to the Matrigel surface or to other macrophages, any cells within  $25 \mu\text{m}$  of the Matrigel surface were excluded from analysis. The protease inhibitor cocktail was prepared from the Sigma Protease Inhibitor Cocktail P1860 (aprotinin, bestatin, E-64, leupeptin and pepstatin A) supplemented with  $5 \mu\text{M}$  GM 6001 (EMD Millipore).

**3D collagen migration assays.** Collagen matrices were prepared from Nutragen type I bovine collagen (Advanced BioMatrix) in  $1 \times$  MEM Eagle supplemented with 7.5% sodium bicarbonate (pH 9) in optical-grade black 96-well plates. Matrices were allowed to polymerize at  $37^\circ\text{C}$  for 60 min to overnight, and then equilibrated for  $\geq 60$  min in monocyte growth media supplemented with 3% serum. In each well,  $5 \times 10^4$  monocytes or macrophages pre-labelled with Cell Trace CFSE (Invitrogen) and pre-infected with *T. gondii* (THP-1: MOI of 4.5 with ME49-mCherry, 4 h; RAW 264.7: MOI of 3 with ME49-mCherry) were allowed to migrate into the matrix. After overnight migration at  $37^\circ\text{C}$  and 5%  $\text{CO}_2$ , the samples were rinsed with PBS and fixed with 4% formaldehyde. Z-stack image series of the monocytes captured within the collagen matrices were captured with the above-described spinning disk microscopy system and an EC Plan-Neofluar  $\times 10$  (NA 0.30) objective. Volocity software was used to generate 3D renderings of the Z-stacks and locate each monocyte using an automated Object Finding protocol based on fluorescence intensity and cell size. Vertical distance migrated was calculated as the distance between the centroid of the cell with the highest Z-position and every other cell.

**Harvest of ex vivo dermal ear tissue and video microscopy of macrophage migration.** Ventral ear sheets were harvested from 7–8-week old female BALB/C mice (Charles River Lab) and stained for laminin (Sigma Aldrich) with Alexa Fluor 555-conjugated secondary antibody as previously described<sup>29</sup>. GFP-expressing RAW macrophages were pre-infected for 3–5 h with ME49-mCherry parasites or IC buffer control, and then harvested by gentle scraping. Infected and uninfected macrophages were mixed together and given 20 min to crawl into the dorsal side of an ear sheet. Ear sheets were then rinsed and imaged dorsal-side down in a temperature-controlled ( $37^\circ\text{C}$ ) and  $\text{CO}_2$ -controlled (5%) chamber and the inverted spinning disk microscope with a  $\times 20$  EC Plan-Neofluar objective (NA 0.50). Videos were collected for 2 h at 3-min intervals, each with Z-stacks spanning 50–80  $\mu\text{m}$  in 5- $\mu\text{m}$  increments. Zen (Zeiss) software was used to correct drift with the Time Alignment function and deconvolve images with a regularized inverse filter and zero-order g-difference<sup>53</sup>. A Volocity automated protocol was used to track all macrophages. Every macrophage track was manually examined to confirm track accuracy and infection status.

**Statistical analysis.** Data sets were analysed in Prism 7 (Graphpad). Normally distributed data were analysed with one-way analysis of variance (ANOVA) and Holm–Sidak's multiple comparison test. Non-normally distributed data were analysed with Kruskal–Wallis test and Dunn's multiple comparison test. Whenever applicable, two-tailed *P* values were calculated and corrected for multiple comparisons. Two-photon data were analysed in Motility Lab (<http://2ptrack.net/>) using two-tailed Wilcoxon tests to assess significance.

**Reporting Summary.** Further information on research design is available in the Nature Research Reporting Summary linked to this article.

## Data availability

All data generated and analysed during this study are included within the paper and the associated Supplementary Information.

Received: 18 October 2018; Accepted: 5 June 2019;  
Published online: 22 July 2019

## References

- Montoya, J. G. & Liesenfeld, O. Toxoplasmosis. *Lancet* **363**, 1965–1976 (2004).
- Santiago-Tirado, F. H. & Doering, T. L. False friends: phagocytes as Trojan horses in microbial brain infections. *PLoS Pathog.* **13**, e1006680 (2017).

3. Harker, K. S., Ueno, N. & Lodoen, M. B. *Toxoplasma gondii* dissemination: a parasite's journey through the infected host. *Parasite Immunol.* **37**, 141–149 (2015).
4. Dubey, J. P. Bradyzoite-induced murine toxoplasmosis: stage conversion, pathogenesis, and tissue cyst formation in mice fed bradyzoites of different strains of *Toxoplasma gondii*. *J. Eukaryot. Microbiol.* **44**, 592–602 (1997).
5. Dubey, J. P., Speer, C. A., Shen, S. K., Kwok, O. C. & Blixt, J. A. Oocyst-induced murine toxoplasmosis: life cycle, pathogenicity, and stage conversion in mice fed *Toxoplasma gondii* oocysts. *J. Parasitol.* **83**, 870–882 (1997).
6. Gregg, B. et al. Replication and distribution of *Toxoplasma gondii* in the small intestine after oral infection with tissue cysts. *Infect. Immun.* **81**, 1635–1643 (2013).
7. Joeris, T., Muller-Luda, K., Agace, W. W. & Mowat, A. M. Diversity and functions of intestinal mononuclear phagocytes. *Mucosal Immunol.* **10**, 845–864 (2017).
8. Dunay, I. R. et al. Gr1<sup>+</sup> inflammatory monocytes are required for mucosal resistance to the pathogen *Toxoplasma gondii*. *Immunity* **29**, 306–317 (2008).
9. Konradt, C. et al. Endothelial cells are a replicative niche for entry of *Toxoplasma gondii* to the central nervous system. *Nat. Microbiol.* **1**, 16001 (2016).
10. Ley, K., Laudanna, C., Cybulsky, M. I. & Nourshargh, S. Getting to the site of inflammation: the leukocyte adhesion cascade updated. *Nat. Rev. Immunol.* **7**, 678–689 (2007).
11. Courret, N. et al. CD11c- and CD11b-expressing mouse leukocytes transport single *Toxoplasma gondii* tachyzoites to the brain. *Blood* **107**, 309–316 (2006).
12. Ueno, N. et al. Real-time imaging of *Toxoplasma*-infected human monocytes under fluidic shear stress reveals rapid translocation of intracellular parasites across endothelial barriers. *Cell. Microbiol.* **16**, 580–595 (2014).
13. Lambert, H., Dellacasa-Lindberg, I. & Barragan, A. Migratory responses of leukocytes infected with *Toxoplasma gondii*. *Microbes Infect.* **13**, 96–102 (2011).
14. Ueno, N. & Lodoen, M. B. From the blood to the brain: avenues of eukaryotic pathogen dissemination to the central nervous system. *Curr. Opin. Microbiol.* **26**, 53–59 (2015).
15. Cook, J. H., Ueno, N. & Lodoen, M. B. *Toxoplasma gondii* disrupts  $\beta$ 1 integrin signaling and focal adhesion formation during monocyte hypermotility. *J. Biol. Chem.* **293**, 3374–3385 (2018).
16. Harker, K. S. et al. *Toxoplasma gondii* modulates the dynamics of human monocyte adhesion to vascular endothelium under fluidic shear stress. *J. Leukoc. Biol.* **93**, 789–800 (2013).
17. Olafsson, E. B., Varas-Godoy, M. & Barragan, A. *Toxoplasma gondii* infection shifts dendritic cells into an amoeboid rapid migration mode encompassing podosome dissolution, secretion of TIMP-1, and reduced proteolysis of extracellular matrix. *Cell. Microbiol.* **20**, e12808 (2018).
18. Lambert, H., Vutova, P. P., Adams, W. C., Loré, K. & Barragan, A. The *Toxoplasma gondii*-shuttling function of dendritic cells is linked to the parasite genotype. *Infect. Immun.* **77**, 1679–1688 (2009).
19. Fuks, J. M. et al. GABAergic signaling is linked to a hypermigratory phenotype in dendritic cells infected by *Toxoplasma gondii*. *PLoS Pathog.* **8**, e1003051 (2012).
20. Weidner, J. M. et al. Rapid cytoskeleton remodelling in dendritic cells following invasion by *Toxoplasma gondii* coincides with the onset of a hypermigratory phenotype. *Cell. Microbiol.* **15**, 1735–1752 (2013).
21. Daniels, B. P. et al. Immortalized human cerebral microvascular endothelial cells maintain the properties of primary cells in an in vitro model of immune migration across the blood brain barrier. *J. Neurosci. Methods* **212**, 173–179 (2013).
22. van Kooyk, Y. & Figdor, C. G. Avidity regulation of integrins: the driving force in leukocyte adhesion. *Curr. Opin. Cell Biol.* **12**, 542–547 (2000).
23. Onken, M. D. et al. Endothelial monolayers and transendothelial migration depend on mechanical properties of the substrate. *Cytoskeleton (Hoboken)* **71**, 695–706 (2014).
24. Belin, B. J., Goins, L. M. & Mullins, R. D. Comparative analysis of tools for live cell imaging of actin network architecture. *Bioarchitecture* **4**, 189–202 (2014).
25. Charras, G. & Paluch, E. Blebs lead the way: how to migrate without lamellipodia. *Nat. Rev. Mol. Cell Biol.* **9**, 730–736 (2008).
26. Lämmermann, T. et al. Rapid leukocyte migration by integrin-independent flowing and squeezing. *Nature* **453**, 51–55 (2008).
27. Kanatani, S., Uhlen, P. & Barragan, A. Infection by *Toxoplasma gondii* induces amoeboid-like migration of dendritic cells in a three-dimensional collagen matrix. *PLoS ONE* **10**, e0139104 (2015).
28. Wolf, K. et al. Collagen-based cell migration models in vitro and in vivo. *Semin. Cell Dev. Biol.* **20**, 931–941 (2009).
29. Weber, M. & Sixt, M. Live cell imaging of chemotactic dendritic cell migration in explanted mouse ear preparations. *Methods Mol. Biol.* **1013**, 215–226 (2013).
30. Cougoule, C. et al. Blood leukocytes and macrophages of various phenotypes have distinct abilities to form podosomes and to migrate in 3D environments. *Eur. J. Cell Biol.* **91**, 938–949 (2012).
31. Van Goethem, E., Poincloux, R., Gauffre, F., Maridonneau-Parini, I. & Le Cabec, V. Matrix architecture dictates three-dimensional migration modes of human macrophages: differential involvement of proteases and podosome-like structures. *J. Immunol.* **184**, 1049–1061 (2010).
32. Lämmermann, T. & Germain, R. N. The multiple faces of leukocyte interstitial migration. *Semin. Immunopathol.* **36**, 227–251 (2014).
33. Shang, X. et al. Rational design of small molecule inhibitors targeting RhoA subfamily Rho GTPases. *Chem. Biol.* **19**, 699–710 (2012).
34. Martiny-Baron, G. et al. Selective inhibition of protein kinase C isozymes by the indolocarbazole Go 6976. *J. Biol. Chem.* **268**, 9194–9197 (1993).
35. Rizvi, S. A. et al. Identification and characterization of a small molecule inhibitor of formin-mediated actin assembly. *Chem. Biol.* **16**, 1158–1168 (2009).
36. Nolen, B. J. et al. Characterization of two classes of small molecule inhibitors of Arp2/3 complex. *Nature* **460**, 1031–1034 (2009).
37. Hunter, C. A. & Sibley, L. D. Modulation of innate immunity by *Toxoplasma gondii* virulence effectors. *Nat. Rev. Microbiol.* **10**, 766–778 (2012).
38. Hakimi, M. A., Olias, P. & Sibley, L. D. *Toxoplasma* effectors targeting host signaling and transcription. *Clin. Microbiol. Rev.* **30**, 615–645 (2017).
39. Etheridge, R. D. et al. The *Toxoplasma* pseudokinase ROP5 forms complexes with ROP18 and ROP17 kinases that synergize to control acute virulence in mice. *Cell Host Microbe* **15**, 537–550 (2014).
40. Hodge, R. G. & Ridley, A. J. Regulating Rho GTPases and their regulators. *Nat. Rev. Mol. Cell Biol.* **17**, 496–510 (2016).
41. Talevich, E. & Kannan, N. Structural and evolutionary adaptation of rhopty kinases and pseudokinases, a family of coccidian virulence factors. *BMC Evol. Biol.* **13**, 117 (2013).
42. Guilluy, C., Garcia-Mata, R. & Burridge, K. Rho protein crosstalk: another social network? *Trends Cell Biol.* **21**, 718–726 (2011).
43. Fox, B. A. et al. The *Toxoplasma gondii* Rhopty kinase is essential for chronic infection. *mBio* **7**, e00193-16 (2016).
44. Swirski, F. K. et al. Identification of splenic reservoir monocytes and their deployment to inflammatory sites. *Science* **325**, 612–616 (2009).
45. Renkawitz, J. & Sixt, M. Mechanisms of force generation and force transmission during interstitial leukocyte migration. *EMBO Rep.* **11**, 744–750 (2010).
46. Hakansson, S., Charron, A. J. & Sibley, L. D. *Toxoplasma* evacuoles: a two-step process of secretion and fusion forms the parasitophorous vacuole. *EMBO J.* **20**, 3132–3144 (2001).
47. Panas, M. W. et al. Translocation of dense granule effectors across the parasitophorous vacuole membrane in *Toxoplasma*-infected cells requires the activity of ROP17, a rhopty protein kinase. Preprint at <https://doi.org/10.1101/613208> (2019).
48. Weksler, B. B. et al. Blood-brain barrier-specific properties of a human adult brain endothelial cell line. *FASEB J.* **19**, 1872–1874 (2005).
49. Kreisel, D. et al. In vivo two-photon imaging reveals monocyte-dependent neutrophil extravasation during pulmonary inflammation. *Proc. Natl Acad. Sci. USA* **107**, 18073–18078 (2010).
50. Zinselmeyer, B. H. et al. Chapter 16. Two-photon microscopy and multidimensional analysis of cell dynamics. *Methods Enzymol.* **461**, 349–378 (2009).
51. Kowarz, E., Loscher, D. & Marschalek, R. Optimized Sleeping Beauty transposons rapidly generate stable transgenic cell lines. *Biotechnol. J.* **10**, 647–653 (2015).
52. Alaganan, A., Fentress, S. J., Tang, K., Wang, Q. & Sibley, L. D. *Toxoplasma* GRA7 effector increases turnover of immunity-related GTPases and contributes to acute virulence in the mouse. *Proc. Natl Acad. Sci. USA* **111**, 1126–1131 (2014).
53. Schaefer, L. H., Schuster, D. & Herz, H. Generalized approach for accelerated maximum likelihood based image restoration applied to three-dimensional fluorescence microscopy. *J. Microsc.* **204**, 99–107 (2001).

## Acknowledgements

We thank J. A. Cooper for constructive comments; R. Klein and T. Doering for sharing the hCMEC/D3 cells; T. Fehniger for facilitating the acquisition of primary human monocytes; F. Santiago and H. Salimi for advice regarding the BBB model; S. Kim, L. Yang and the Washington University School of Medicine In vivo Imaging Core for technical support and fluorescent reporter mice for the intravital imaging experiments;

and G. Randolph for generously sharing the CX<sub>3</sub>CR1<sup>GFP/+</sup> mice. Work was supported in part by grants from the National Science Foundation to L.L.D. (DGE-1143954), and from the National Institutes of Health to M.J.M. (R01AI077600) and L.D.S. (AI034036).

### Author contributions

L.L.D. and L.D.S. designed the experiments and wrote the manuscript. N.G.J. generated the *T. gondii* strains used for time-lapse microscopy. Q.W. collaborated on the design and execution of animal studies. M.D.O. collaborated on the design and interpretation of the Rho GTPase inhibitor studies. L.L.D. and M.J.M. designed and performed the two-photon imaging experiments. L.L.D. performed all other experiments and analysed the data. L.D.S. supervised the study. All authors critically reviewed and approved the manuscript.

### Competing interests

The authors declare no competing interests.

### Additional information

**Supplementary information** is available for this paper at <https://doi.org/10.1038/s41564-019-0504-8>.

**Reprints and permissions information** is available at [www.nature.com/reprints](http://www.nature.com/reprints).

**Correspondence and requests for materials** should be addressed to L.D.S.

**Publisher's note:** Springer Nature remains neutral with regard to jurisdictional claims in published maps and institutional affiliations.

© The Author(s), under exclusive licence to Springer Nature Limited 2019

## Reporting Summary

Nature Research wishes to improve the reproducibility of the work that we publish. This form provides structure for consistency and transparency in reporting. For further information on Nature Research policies, see [Authors & Referees](#) and the [Editorial Policy Checklist](#).

### Statistical parameters

When statistical analyses are reported, confirm that the following items are present in the relevant location (e.g. figure legend, table legend, main text, or Methods section).

n/a | Confirmed

- The exact sample size ( $n$ ) for each experimental group/condition, given as a discrete number and unit of measurement
- An indication of whether measurements were taken from distinct samples or whether the same sample was measured repeatedly
- The statistical test(s) used AND whether they are one- or two-sided  
*Only common tests should be described solely by name; describe more complex techniques in the Methods section.*
- A description of all covariates tested
- A description of any assumptions or corrections, such as tests of normality and adjustment for multiple comparisons
- A full description of the statistics including central tendency (e.g. means) or other basic estimates (e.g. regression coefficient) AND variation (e.g. standard deviation) or associated estimates of uncertainty (e.g. confidence intervals)
- For null hypothesis testing, the test statistic (e.g.  $F$ ,  $t$ ,  $r$ ) with confidence intervals, effect sizes, degrees of freedom and  $P$  value noted  
*Give  $P$  values as exact values whenever suitable.*
- For Bayesian analysis, information on the choice of priors and Markov chain Monte Carlo settings
- For hierarchical and complex designs, identification of the appropriate level for tests and full reporting of outcomes
- Estimates of effect sizes (e.g. Cohen's  $d$ , Pearson's  $r$ ), indicating how they were calculated
- Clearly defined error bars  
*State explicitly what error bars represent (e.g. SD, SE, CI)*

*Our web collection on [statistics for biologists](#) may be useful.*

### Software and code

Policy information about [availability of computer code](#)

Data collection

Zen Blue version 2 (Zeiss), Gen 5 version 2.09 (BioTek), Slidebook (Intelligent Imaging Solutions), Xenogen Living Image (Caliper Life Sciences)

Data analysis

Gen 5 version 2.09 (BioTek), Volocity version 6.3 (Perkin Elmer), Prism version 7 (Graphpad), Excel 2016 (Microsoft), Imaris version 9 (Bitplane), Motility Lab (2ptrack.net)

For manuscripts utilizing custom algorithms or software that are central to the research but not yet described in published literature, software must be made available to editors/reviewers upon request. We strongly encourage code deposition in a community repository (e.g. GitHub). See the Nature Research [guidelines for submitting code & software](#) for further information.

### Data

Policy information about [availability of data](#)

All manuscripts must include a [data availability statement](#). This statement should provide the following information, where applicable:

- Accession codes, unique identifiers, or web links for publicly available datasets
- A list of figures that have associated raw data
- A description of any restrictions on data availability

All data associated with this study are included within the paper and supplementary information.

## Field-specific reporting

Please select the best fit for your research. If you are not sure, read the appropriate sections before making your selection.

Life sciences  Behavioural & social sciences  Ecological, evolutionary & environmental sciences

For a reference copy of the document with all sections, see [nature.com/authors/policies/ReportingSummary-flat.pdf](https://www.nature.com/authors/policies/ReportingSummary-flat.pdf)

## Life sciences study design

All studies must disclose on these points even when the disclosure is negative.

Sample size	Samples sizes were chosen to provide an estimate of the sample variance (to determine if parametric vs non-parametric statistical tests were appropriate) and to support appropriate statistical testing for difference in population means or distributions. No formal sample size calculations were performed.
Data exclusions	none
Replication	All in vitro assays were performed multiple times, with each independent experiment including multiple within-experiment biological replicates. All animal studies were performed multiple times, including mouse groups from multiple litters. All experiments were repeated multiple times with similar outcomes and the precise number of biological and technical replicates are provided in each figure legend.
Randomization	For in vitro assays, no randomization was performed as all cells were grown under controlled conditions. For animal experiments using wild-type CD1 mice, age- and sex-matched groups were used. Practical considerations for the multi-photon imaging studies precluded the use of perfectly age- and sex-matched mice; for these studies, mixed sex groups of CX3CR1-gfp/+ mice spanning similar age ranges for each condition were used.
Blinding	Samples were not blinded. Data acquisition and analysis were automated whenever possible.

## Reporting for specific materials, systems and methods

### Materials & experimental systems

n/a	Involvement in the study
<input type="checkbox"/>	<input checked="" type="checkbox"/> Unique biological materials
<input type="checkbox"/>	<input checked="" type="checkbox"/> Antibodies
<input type="checkbox"/>	<input checked="" type="checkbox"/> Eukaryotic cell lines
<input checked="" type="checkbox"/>	<input type="checkbox"/> Palaeontology
<input type="checkbox"/>	<input checked="" type="checkbox"/> Animals and other organisms
<input checked="" type="checkbox"/>	<input type="checkbox"/> Human research participants

### Methods

n/a	Involvement in the study
<input checked="" type="checkbox"/>	<input type="checkbox"/> ChIP-seq
<input type="checkbox"/>	<input checked="" type="checkbox"/> Flow cytometry
<input checked="" type="checkbox"/>	<input type="checkbox"/> MRI-based neuroimaging

## Unique biological materials

Policy information about [availability of materials](#)

Obtaining unique materials

## Antibodies

Antibodies used	mAb 12G10 (Abcam 30394, 1:200 dilution), mAb 24 (Abcam 13219, 1:100 dilution), mAb 9F10 (Biolegend 304301, 1:200 dilution), mAb TS2/4 (Biolegend 350602, 1:500 dilution), polyclonal anti-laminin (Sigma L9393, 1:500 dilution), PE-conjugated anti-human CD33 mAb 67.6 (Stem Cell Tech 60126PE.1, 1:100 dilution), mAb MO563 anti-GRA7 (Alaganaan et al PNAS 2014, 1:1000 dilution), anti-MYC polyclonal (ThermoFisher PA1-981, 1:1000 dilution)
Validation	All antibodies have been previously used for similar applications and validated by manufacturers. Optimal dilution for these studies was determined by titration according to manufacturer-recommended ranges.  mAb 12G10- validated by Abcam for ICC/IF, flow cytometry, ELISA, and western blot mAb 24- validated by Abcam for ICC/IF, flow cytometry, IP, and western blot mAb 9F10- validated by BioLegend for flow cytometry

mAb TS2/4- validated by BioLegend for flow cytometry  
 mAb 67.6- validated by StemCell Tech for flow cytometry and cell isolation  
 anti-MYC polyclonal- validated by ThermoFisher for IF and western blot  
 anti-GRA7 mAb MOS63- see Alaganan et al PNAS 2014

## Eukaryotic cell lines

Policy information about [cell lines](#)

Cell line source(s)	Obtained from ATCC: THP-1, RAW 264.7. Obtained from Robyn Klein Lab (Washington University): hCMEC/D3
Authentication	Cell lines obtained directly from ATCC were not authenticated. hCMEC/D3 analyzed in Daniels et al, J Neurosci Methods 2013.
Mycoplasma contamination	All cell lines tested negative for mycoplasma contamination.
Commonly misidentified lines (See <a href="#">ICLAC</a> register)	None.

## Animals and other organisms

Policy information about [studies involving animals](#); [ARRIVE guidelines](#) recommended for reporting animal research

Laboratory animals	BALB/C mice female 7-8 weeks (Charles River Lab), CD1 mice female 8-10 weeks (Charles River Lab), C57BL/6 CX3CR1-GFP/+ mice male and female 8-16 weeks (Jackson Labs)
Wild animals	No wild animals were used in this study.
Field-collected samples	No field-collected samples were used in this study.

## Flow Cytometry

Plots

Confirm that:

- The axis labels state the marker and fluorochrome used (e.g. CD4-FITC).
- The axis scales are clearly visible. Include numbers along axes only for bottom left plot of group (a 'group' is an analysis of identical markers).
- All plots are contour plots with outliers or pseudocolor plots.
- A numerical value for number of cells or percentage (with statistics) is provided.

Methodology

Sample preparation	Live impermeabilized THP-1 cells were stained on ice with indicated antibodies.
Instrument	BD FACSCanto
Software	FlowJoV10
Cell population abundance	In uninfected samples, >80% of collected events gated as THP-1 cells by FSC/SSC. In infected samples, about 50% of collected events gated as THP-1 cells.
Gating strategy	FSC/SSC was used to gate for viable THP-1 cells, excluding debris and extracellular parasites, see Supplementary Fig 2b.

- Tick this box to confirm that a figure exemplifying the gating strategy is provided in the Supplementary Information.